ACS Photonics

pubs.acs.org/journal/apchd5 Article

Fate of Optical Excitons in $FAPbI_3$ Nanocube Superlattices

Alessandra Milloch,* Umberto Filippi, Paolo Franceschini, Selene Mor, Stefania Pagliara, Gabriele Ferrini, Franco V. A. Camargo, Giulio Cerullo, Dmitry Baranov, Liberato Manna, and Claudio Giannetti*

Cite This: *ACS Photonics* 2024, 11, 3511−3520 Read Online

ACCESS | Metrics & More | Article Recommendations | Supporting Information

ABSTRACT: Understanding the nature of the photoexcitation and ultrafast charge dynamics pathways in organic halide perovskite nanocubes and their aggregation into superlattices is key for potential applications as tunable light emitters, photon-harvesting materials, and light-amplification systems. In this work, we apply two-dimensional coherent electronic spectroscopy (2DES) to track in real time the formation of near-infrared optical excitons and their ultrafast relaxation in $CH(NH_2)_2PbI_3$ nanocube superlattices. Our results unveil that the coherent ultrafast dynamics is limited by the combination of the inherent short exciton decay time (≃40 fs) and the dephasing due to the coupling with selective optical phonon modes at higher temperatures. On the picosecond time scale, we observe the progressive formation of long-lived localized trap states. The analysis of the temperature dependence of the excitonic intrinsic line width, as extracted by the antidiagonal components of the 2D spectra, unveils a dramatic change of the excitonic coherence time across the cubic to tetragonal structural transition. Our results offer a new way to control and enhance the ultrafast coherent dynamics of photocarrier generation in hybrid halide perovskite synthetic solids.

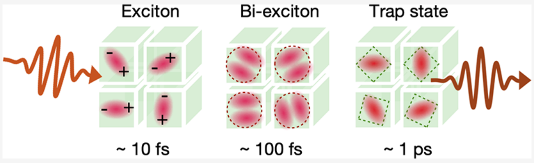

KEYWORDS: *hybrid halide perovskites, nanocube superlattices, 2D spectroscopy, multiexciton dynamics, trap states*

■ INTRODUCTION

Lead halide perovskites, thanks to their outstanding optical and electronic properties,[1−3] are ideal materials for a wide variety of applications ranging from optoelectronics to photovoltaics.[3,4] The recent advances in the synthesis of hybrid halide perovskite nanocubes[5] have enabled unprecedented control of the emission properties by combining the tunability of the chemical composition with that of the nanocube shape and size. The further advance given by the synthesis of nanocube superlattices (Figure 1a)[6−8] not only provides additional control parameters, such as the superlattice size, periodicity, and structure,[9] but also paves the way to the development of novel light-emitting devices based on cooperative superradiant effects,[10−13] as well as to the implementation of quantum simulators of solid state problems.[14] Collective superradiant phenomena in nanocube superlattices are driven by the long-range electromagnetic interactions among excitons in different nanocubes[15−17] and are therefore crucially affected by the exciton dynamics following light excitation of the individual nanocubes.[18] Light emission in lead halide perovskites can also be affected by the strong coupling of excitons with the lattice, which results in broad spectra originating from self-trapped exciton (STE) states.[19,20]

An important case is given by hybrid organic−inorganic halide perovskite superlattices, whose excitonic energy extends down to the near-infrared (1.5 eV), thus, significantly broadening the potential exploitation of these synthetic materials.[5,21−23] Formamidinium lead iodide $FAPbI_3$ (FAPI, $FA^+ = CH(NH_2)_2{}^+$) is especially promising because of its smaller band gap and increased chemical and thermal stability as compared to the archetypal compound MAPI ($MA^+ = CH^3NH^{3+}$).[24−26] In these systems, the presence of collective superradiance effects, analogous to those reported in fully inorganic superlattices, remains unclear; the possibility of extending superradiant phenomena to hybrid organic−inorganic perovskite superlattices requires an understanding of the ultrafast exciton dynamics of these systems. The photophysics of these materials is in fact characterized by a complex interplay of free carrier excitations, bound excitons, multiexcitons, and trapped states, which generally give rise to multiple optical resonances in the visible/near-infrared range. These resonances overlap in energy and cannot be disentangled by linear or pump−probe spectroscopies. In Figure 1b, for example, we report a typical absorption spectrum of FAPI superlattices which shows multiple features compatible with the existence of multiple excitonic-like resonances in the 1.6−1.8 eV range (see Supporting Information, Section S1-D, for details of the analysis and

Received: January 17, 2024
Revised: July 18, 2024
Accepted: July 18, 2024
Published: September 4, 2024

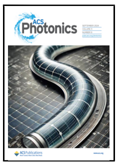

https://doi.org/10.1021/acsphotonics.4c00105

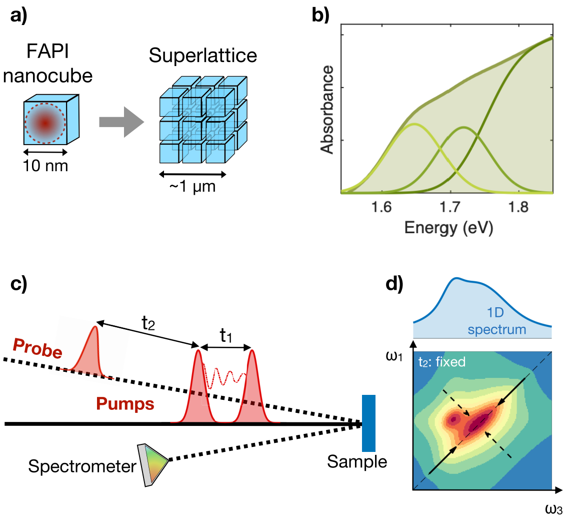

Figure 1. (a) Cartoon of FAPI nanocubes, hosting quantum confined excitons, and FAPI superlattices. (b) Absorption spectrum (green area) of the FAPI superlattices sample measured in this work. The green solid lines represent a free carriers edge and two peaks, as obtained from Elliott analysis of the room temperature absorbance (Supporting Information, Section S1-D). (c) Scheme of 2DES experiment. (d) Sketch of a typical 2D spectrum (vertical axis: excitation, horizontal axis: detection) where, as opposed to 1D experiments (top panel), homogeneous and inhomogeneous line widths and correlations between spectral features can be resolved.

fitting of the linear spectra). Due to the overlap of different structures, however, a linear fit can hardly offer a decisive answer regarding the nature of the absorption. Therefore, the nature of the photocarrier generation and recombination processes in hybrid halide perovskite superlattices is still a matter of debate.[27−30] Since addressing the early stage dynamics of these processes is of central importance for controlling and enhancing macroscopic coherent effects, advanced optical techniques that go beyond linear spectroscopies and combine high temporal and spectral resolution should be employed.[11,31]

In this work, we use two-dimensional coherent electronic spectroscopy (2DES) to investigate the exciton dynamics in FAPI nanocube superlattices. 2DES allows us to unveil the hierarchy of the photoexcitation and relaxation processes. We report evidence of early stage excitons which rapidly decay and form novel bound states compatible with biexcitons, both at room temperature and at cryogenic temperatures. Within a few hundred femtoseconds, the excitonic resonance is lost in favor of the generation of lower energy trap-states ascribable to self-trapping of excitons or defect-trapping.[19] Analysis of the excitonic decoherence times suggests that coherent ultrafast diffusion is limited by the short exciton lifetime at cryogenic temperatures and that the interaction with optical phonon modes starts to play a role at higher temperatures. The exciton decoherence time is also directly affected by the tetragonal-to-cubic phase transition occurring upon raising the temperature: the symmetry increase suppresses the number of optical phonon modes, thus offering a new parameter for controlling the photoconversion process and the onset of coherent phenomena. Overall, these results provide a snapshot of the ultrafast exciton dynamics in FAPI nanocubes deposited on a solid substrate, which is key for future modeling and control of possible collective properties emerging in more complex structures, such as superlattice with different symmetries or twisted 2D-perovskites configurations.[9,32]

■ EXPERIMENTAL SECTION

2DES[33−35] is a multidimensional approach based on the use of a pair of phase-coherent broadband excitation pulses (see Figure 1c), separated by a variable time delay t_1 (coherence time) and a probe pulse delayed by t_2 (waiting time) to measure the transient reflectivity/transmissivity of the sample. Spectral resolution along the excitation axis is achieved by Fourier transforming the signal with respect to t_1, while resolution along the detection axis is achieved by spectrally resolving the detection of the signal.[36,37] The 2DES setup adopted here is based on the Translating-Wedge-Based Identical Pulses eNcoding System (TWINS) scheme.[38] As detailed in Materials and Methods, two common-path birefringent interferometers are employed: the first interferometer (GEMINI 2D by NIREOS) generates the pair of collinear phase-coherent pump pulses,[39] the second one (GEMINI by NIREOS) is used in detection to spectrally resolve the transient reflectivity measured by the probe.[40] The partially collinear geometry employed here (see Materials and Methods and Supporting Information, Section S2, for experimental details) measures the purely absorptive spectrum

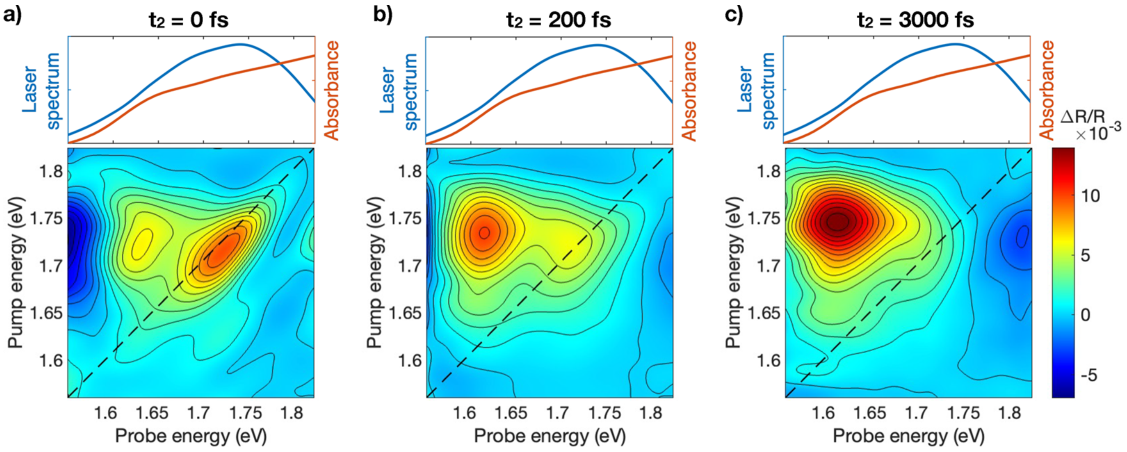

Figure 2. 2D spectra of the FAPI superlattice measured at 200 K with 175 μJ/cm^2 excitation fluence for three different t_2 delays: (a) t_2 = 0 fs, (b) 200 fs, and (c) 3 ps. The top panels show the sample absorption spectrum (red) and the laser pulse spectrum (blue).

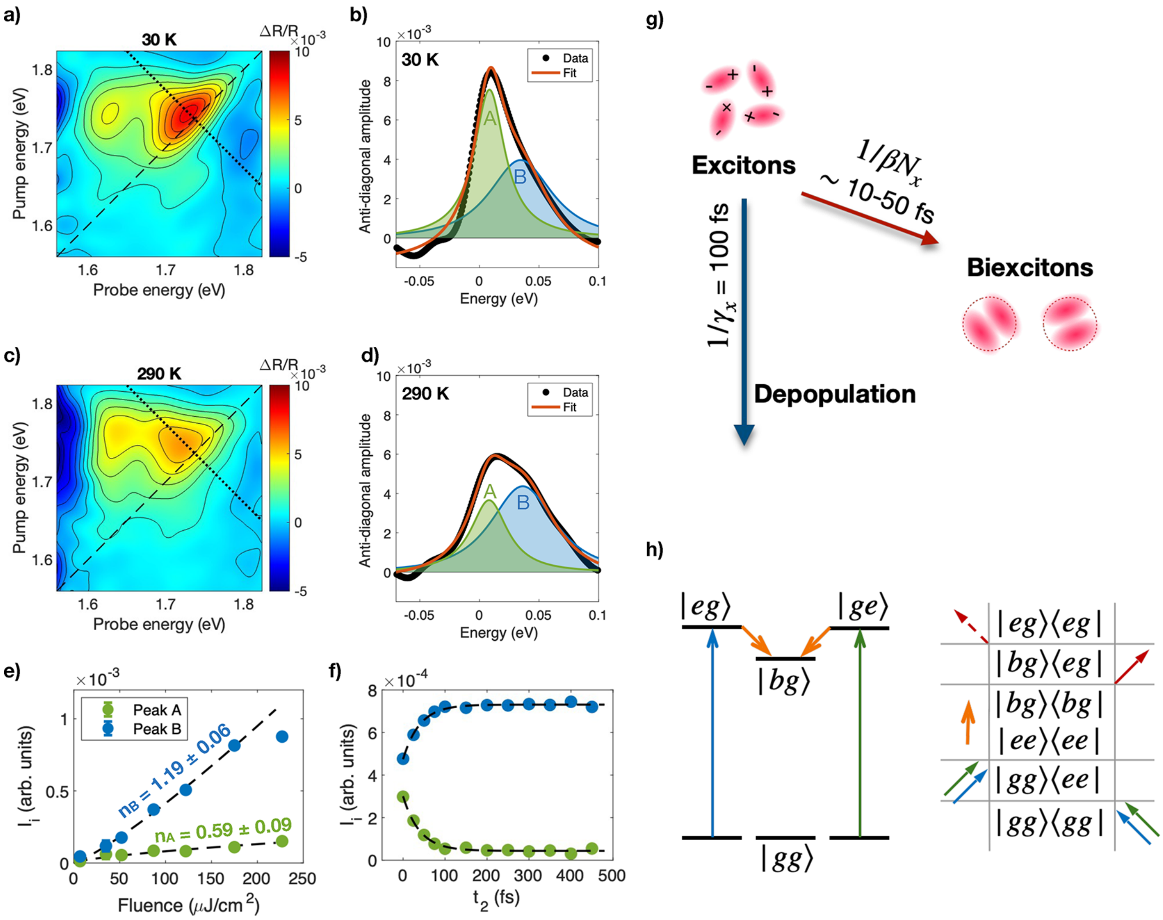

Figure 3. (a) 2D spectrum of FAPI superlattices measured at 30 K and $t_2 = 0$ fs, with 175 μJ/cm^2 excitation fluence. (b) Antidiagonal profile of the 2D spectrum in (a) taken along the dotted line in (a). The black dots are the experimental data points, the red line is the profile fit, and the green and blue filled areas are peaks A and B associated with, respectively, exciton and biexciton resonances. (c) and (d) display a 2D spectrum and an antidiagonal profile analogous to (a) and (b), but collected at a higher sample temperature (290 K). (e) Fluence dependence of the integrated amplitude I_i of peaks A and B, extracted from fitting the 2D spectra antidiagonal profiles at 200 K and $t_2 = 0$ fs. The black dashed lines represent the power-law fit to the data. (f) Dynamics of the exciton (peak A) and biexciton (peak B) peak amplitudes I_i at 200 K for 175 μJ/cm^2 excitation fluence. (g) Sketch of the relaxation channels for excitons, which can decay at a γ_x rate or bind into biexcitons at a rate βN_x, N_x being the instantaneous number of excitons. (h) Representation of the energy levels scheme (left) and fifth-order rephasing double-sided Feynman diagrams (right) for the biexciton formation process.

which corresponds to the sum of the real part of rephasing and nonrephasing signals.[36] This technique allows to detect, for each t_2 delay, a two-dimensional map which connects excitation at a given frequency ω_1 to the response of the system at another frequency ω_3, while retaining the femtosecond temporal resolution given by the pulse duration. The 2D spectra allow to disentangle the intrinsic decoherence dynamics of optical excitations, which manifest as a broadening along the antidiagonal direction (see Figure 1d), from disorder-induced inhomogeneous broadening along the diagonal of the ω_1−ω_3 map. By monitoring the temporal evolution of different peaks in the map, it is also possible to infer a cause-effect relationship between different spectral features. This capability is key for monitoring the real-time transformation of the initial photoexcited carriers into the long-lived states responsible for the slow fluorescence emission.

The FAPI superlattices investigated in this work are assembled from a colloidal dispersion of uniform ∼10 nm nanocubes. The studied samples comprise ∼0.3−1 μm superlattices of close-packed nanocubes deposited on a silicon substrate (see Materials and Methods for sample preparation details). The 2DES spectra are collected in the reflection geometry, which guarantees a better signal-to-noise ratio compared to the transmission configuration (Supporting Information, Section S6).

RESULTS AND DISCUSSION

In Figure 2 we report the spectra measured on FAPI superlattices at $T = 200$ K as a function of the excitation ($\hbar\omega_1$, vertical axis) and detection ($\hbar\omega_3$, horizontal axis) photon energies and for different t_2 delays. They display two distinct spectral features: (i) a component located along the diagonal of the spectrum around 1.72 eV (Figure 2a), (ii) a broad structure centered off-diagonal, at $\hbar\omega_1 \simeq 1.72$ eV pump photon energy and $\hbar\omega_3 \simeq 1.61$ eV probe photon energy (Figure 2b,c), which can be ascribed to transient photobleaching and stimulated emission (see also the positive transmissivity variation reported in the Supporting Information, Section S6). As observed from 2D spectra at different t_2 time delays, these two spectral features are characterized by different dynamics, with feature (i) decaying on a subpicosecond time scale and feature (ii) building up on a longer time scale. The well-defined and well-localized diagonal structure reveals the existence in FAPI superlattices of a short-lived bound exciton at 1.72 eV, whereas the delayed off-diagonal feature suggests the formation of long-lived trap-states. In the following, we analyze in detail the characteristics of these two components.

We first examine the short time delay (t_2 = 0 fs) 2D spectrum and investigate the temperature dependence of the excitonic peak. The elongation along the diagonal of the 2D spectrum allows estimating the inhomogeneous full width at half maximum (fwhm) that results in ≃83 ± 4 meV when projected along the probe axis. This value is compatible with the width of the resonance at 1.72 eV in the steady state absorbance (Supporting Information, Section S1-D). The large inhomogeneous broadening originates from the size and shape dispersion of FAPI nanocubes and superlattices. The intrinsic homogeneous line width can instead be obtained from slicing the 2D spectrum measured at t_2 = 0 fs along the antidiagonal direction crossing the exciton peak (see dotted lines in Figure 3a,c). The resulting antidiagonal cuts are plotted in Figure 3b and d for experiments conducted at two different temperatures; the horizontal axis represents the energy axis along the antidiagonal direction, with positive values referring to the region above the diagonal in the 2D spectra (i.e., the region corresponding to pump photon energy larger than probe energy). The antidiagonal profiles so obtained show a clear asymmetry that reveals the existence of two structures, one centered on the 2D spectrum diagonal (peak A) and one located above the diagonal (peak B). We stress that the signal acquired in a conventional pump−probe experiment, which corresponds to integrating along the $\hbar\omega_1$ axis (see Figure 1c), would be dominated by the large inhomogeneous broadening of the exciton, thus preventing the possibility of inferring information about the decoherence and the emergence of secondary structures.

A multipeak fitting, described in detail in Supporting Information, Section S4, is performed in order to extract the peak amplitudes I_i, line widths Γ_i, and positions $x_{0,i}$, where i = A and B (see Section S4 for the detailed list of values). In order to assess the origin of these two components, we perform fluence-dependent and time-resolved (t_2 dependence) 2DES at T = 200 K. In Figure 3e we report the peak amplitudes (integrated areas along the antidiagonal line-cut) as a function of the incident light fluence F. The power law $I_i = cF^{n_i}$ is fit to the data to determine possible nonlinearities, c being a free coefficient. We observe that the peak amplitudes clearly display two different behaviors: I_A scales sublinearly with the fluence ($n_A = 0.59 \pm 0.09$), whereas I_B follows a superlinear power law ($n_B = 1.19 \pm 0.06$), before saturating at large excitation intensity. From the t_2 scan between 0 and 450 fs (Figure 3f), we observe a fast decay of $I_A(t_2)$, counterbalanced by an increase of $I_B(t_2)$. This behavior indicates that spectral weight transfers from peak A to peak B within tens of femtoseconds. To quantitatively analyze the I_i dynamics, we fit the data using the following exponential laws: $I_A(t_2) = I_{A0}\exp(-t_2/\tau_A) + I_{A\infty}$ and $I_B(t_2) = I_{B0} + K[1 - \exp(-t_2/\tau_B)]$. The best fit to the data returns $\tau_A = \tau_B = 39 \pm 6$ fs and $K \simeq I_{A0}$, thus indicating the same time constant for the two processes and the conservation of the total spectral weight ($I_A(t_2) + I_B(t_2) = \mathit{constant}$ for any delay t_2). The constant $I_{A\infty}$ in $I_A(t_2)$ accounts for a slow exciton decay occurring over a time scale that is longer than the t_2 range scanned here. Investigation of the dynamics of peak B on time scales longer than 500 fs is hindered by the appearance of the strong and broad off-diagonal structure. These results indicate that peak B corresponds to a new bound state that is formed following the photoinjection of excitons. One possible scenario is that peak B arises from the formation of biexcitons that can live on a longer time scale.[41] Occupation of the biexciton state, i.e., a bound state originating from the interaction between two excitons and resulting in a lower energy state, gives rise to a transient signal at a probe photon energy smaller than the excitation energy, which corresponds to an off-diagonal signal at a distance from the diagonal equal to the exciton−exciton binding energy. The energy separation between peak A and peak B, i.e., $x_{0,A}-x_{0,B}$, therefore, provides the exciton−exciton interaction strength, $\delta E_{bi-\mathrm{exc}}$. The estimated value, $\delta E_{bi-\mathrm{exc}} = 29 \pm 4$ meV, is compatible with the biexciton binding energy reported in the literature for similar systems.[42−44] In order to further support this picture, the fluence dependence in Figure 3e and the dynamics in Figure 3f are compared with numerical solutions of exciton and biexciton rate equations, discussed in Supporting Information, Section S3. The rate equation model shows that both the experimental t_2-dynamics and the power-law exponents of peaks A and B are compatible with the behavior expected for exciton decay and biexciton formation originating from exciton−exciton interaction. More specifically, the rate equations model that reproduces the experimental trends provides an out-of-equilibrium scenario where photoinjected excitons are subject to multiple decay channels, as sketched in Figure 3g. The excitonic population decays at a rate γ_x, which effectively includes all the direct depopulation channels, including relaxation to the ground state, formation of trap states and any mechanism that changes the exciton density; at the same time, exciton−exciton interaction leads to the formation of the biexciton bound states, which takes place at a rate βN_x, where N_x is the instantaneous number of excitons and β is a fit parameter. The parameters that better match the experimental findings suggest that direct excitonic decay takes place on a time scale of the order of γ_x^{-1} = 100 fs, whereas the biexciton formation rate, which depends on the product βN_x (N_x being the instantaneous number of excitons) strongly depends on the time considered. In the early stage dynamics (10−50 fs), the biexciton production characteristic time spans a $1/\beta N_x$ = 10−70 fs range. This indicates that the generation of biexcitonic bound states occurs already within the 30 fs duration of both the pump and probe pulses. The formation of biexcitons necessarily corresponds to fifth-order or higher nonlinear signals, since the generation of each exciton requires two field−matter interactions. In order to represent such a process, we describe the system with a density matrix that can describe two independent exciton states, $|eg\rangle\langle eg|$ and $|ge\rangle\langle ge|$ (the labels e and g indicate exciton and ground state, respectively), which account for the third order response, as well as two interacting exciton states, $|ee\rangle\langle ee|$, which account for the fifth-order response.[45,46] The interacting excitons can then form the biexciton state, which is represented by $|bg\rangle\langle bg|$ (the label b refers to biexciton) and lead to a red-shifted signal due to the biexciton binding energy. Figure 3h shows a possible rephasing Feynman diagram representing this process that is phase-matched in the direction of the probe pulses. The pathway displayed in Figure 3h corresponds to a stimulated emission signal, in agreement with 2DES experiments in transmission geometry (Supporting Information, Section S6), which, despite being noisier, show a transient increase of transmission in the energy region corresponding to peak B.

The homogeneous line width Γ_i of exciton and biexciton is estimated by line shape analysis at short time delay t_2. The degree of inhomogeneity of the excitonic resonance under investigation may result in an antidiagonal width that depends not only on the homogeneous broadening but also on inhomogeneous broadening effects.[47] Therefore, an accurate estimate of the homogeneous contribution calls for a simultaneous fit of diagonal and antidiagonal slices of the 2D spectrum.[47,48] The fitting functions for diagonal and antidiagonal slices of the 2D maps can be obtained from the solutions of the optical Bloch equations for a two-level systems with Gaussian inhomogeneous broadening,[47] as discussed in Supporting Information, Section S4. By considering both rephasing and nonrephasing signals, the purely absorptive line shape for the antidiagonal direction at $t_2 = 0$ is given by the real part of

$$\begin{aligned} S^{R}_{\omega_0}(\omega) + S^{NR}_{\omega_0}(\omega) = {} & \frac{1}{\sigma(\Gamma - i\omega)}\exp\left[\frac{(\Gamma - i\omega)^2}{2\sigma^2}\right]\mathrm{erfc}\left[\frac{\Gamma - i\omega}{\sqrt{2}\,\sigma}\right] \\ & + \frac{e^{\Gamma^2/2\sigma^2}}{\sqrt{2}\,\sigma i}\frac{1}{\omega}e^{-\omega^2/2\sigma^2}\left[e^{-i\omega\Gamma/\sigma^2}\mathrm{erfc}\left(\frac{\Gamma - i\omega}{\sqrt{2}\,\sigma}\right)\right. \\ & \left. - e^{i\omega\Gamma/\sigma^2}\mathrm{erfc}\left(\frac{\Gamma + i\omega}{\sqrt{2}\,\sigma}\right)\right] \end{aligned} \qquad (1)$$

where ω is the frequency axis along the antidiagonal direction of the 2D spectrum, ω_0 is the absorption peak central frequency, Γ is the dephasing rate, σ is the inhomogeneous width, and erfc is the complementary error function. Similarly, the diagonal line shape is the real part of

$$\begin{aligned} S^{R}_{\omega_0}(\omega') + S^{NR}_{\omega_0}(\omega') = {} & \sqrt{\frac{2}{\pi\sigma^2}}\,e^{-\omega'^2/2\sigma^2} * \frac{1}{\Gamma^2 + \omega'^2} \\ & + \frac{1}{\sigma}e^{-\omega'^2/2\sigma^2} * \frac{1}{(\Gamma + i\omega')^2} \end{aligned} \qquad (2)$$

with ω' frequency axis along the diagonal direction and * indicating the convolution. The simultaneous fit of diagonal and antidiagonal profiles allows to estimate the parameters σ and Γ. Here, we employed this fitting procedure as detailed in Supporting Information, Section S4, which allows us to disentangle, from the measured 2D spectra, the homogeneous line width contribution for both exciton and biexciton resonances. In the following, we will adopt the notations $\Gamma_A = \Gamma_{exc}$ and $\Gamma_B = \Gamma_{bi-exc}$ to directly link to the physical origin of the two structures. The extracted values are plotted in Figure 4a as a function of sample temperature T. At cryogenic temperature, we estimate $\Gamma_{exc} = 15 \pm 2$ meV (obtained from the average value of the three measurements at $T \leq 100$ K), which corresponds to a pure decoherence time $\tau_{dech} = 44 \pm 5$ fs, where $\tau_{dech} = \hbar/\Gamma_{exc}$. This value is of the same order of the $\tau_A \simeq 40$ fs depopulation time, thus suggesting that the leading mechanism determining the homogeneous line width is the decay into biexcitons. The coherent propagation of the excitons is thus limited, even at cryogenic temperatures, by their ultrashort lifetime, preventing the development of delocalized states and superradiant coherent states similar to those observed in inorganic halide perovskite superlattices.[10,14,16] For the biexcitonic state, we obtain $\Gamma_{bi-exc} = 31 \pm 4$ meV between $T = 30$ K and $T = 100$ K, corresponding to $\tau_{dech} = 21 \pm 3$ fs. In this case, the decoherence time scale is much shorter than the biexciton depopulation time, thus indicating the formation of a strongly incoherent gas of interacting biexcitons, surviving for hundreds of femtoseconds.

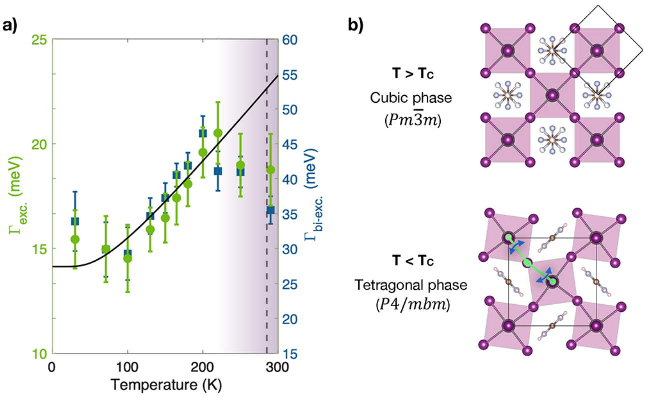

Figure 4. (a) Temperature dependence of the exciton (green circles, left axis) and biexciton (blue squares, right axis) homogeneous line widths extracted from simultaneous fitting of diagonal and antidiagonal profiles at short time delay t_2. The black solid line represents the line width broadening originating from interaction with an optical phonon mode at $E_{OP} = 17$ meV. The purple shaded area represents the temperature range where FAPI nanocubes have cubic lattice structure and where the deviation from the expected temperature-dependent trend is observed. (b) Top panel: FAPI crystal structure in the high-temperature cubic phase with the organic cation subject to orientational disorder. Bottom panel: low-temperature tetragonal phase of the FAPI perovskite. The black squares highlight the unit cell. The green lines and blue arrows indicate the I—Pb—I bending mode that softens in the proximity of the second-order tetragonal-to-cubic phase transition.

The temperature dependence of both Γ_{exc} and Γ_{bi-exc} is reported in Figure 4a (green circles and blue squares, respectively). We observe a similar temperature-dependent line width broadening, which suggests that at higher temperatures the decoherence process is accelerated by the coupling to the thermal bath, consisting of optical phonons. The temperature-dependent increase of $\Gamma_{exc}(T)$ is compared to the thermal broadening (black solid line in Figure 4a) expected for coupling to longitudinal optical phonons, which is described by the function $\Gamma_{exc}(T) = \Gamma_{exc,0} + \Gamma_{OP}/[\exp(E_{OP}/k_BT) - 1]$, where $\Gamma_{exc,0}$ is the intrinsic line width at low-temperature, Γ_{OP} is the exciton-optical phonon coupling coefficient and E_{OP} is the optical phonon energy.[49] According to literature reports, FAPI displays optical phonon modes at energy E_{OP} between 15 and 19 meV,[26,42,50−52] which have been ascribed to vibrations of the organic cation with respect to the inorganic cage.[51,53] These libration modes of the organic cation have also been reported to affect the photoluminescence intensity and the lifetime of photoexcited states in MAPI perovskite.[54] Interaction with such vibrational modes fully accounts for the homogeneous broadening measured in the present work for $T < 250$ K. In this temperature range, fitting of $\Gamma_{exc}(T)$ returns $\Gamma_{exc,0} = 14 \pm 1$ meV and $\Gamma_{OP} = 8 \pm 2$ meV when E_{OP} is fixed to values between 15 to 19 meV.

The temperature-dependent trend suggests that at low temperatures the exciton coherence is mainly limited by the biexciton formation, while at higher temperatures the scattering with thermally activated optical phonons also contributes to faster decoherence. Interestingly, a clear deviation from the trend expected for scattering with thermally activated phonons is observed for temperatures higher than $T^* \simeq 250$ K, where the measured homogeneous line width is smaller than what is expected due to thermal broadening in this temperature range. T^* is very close to the critical

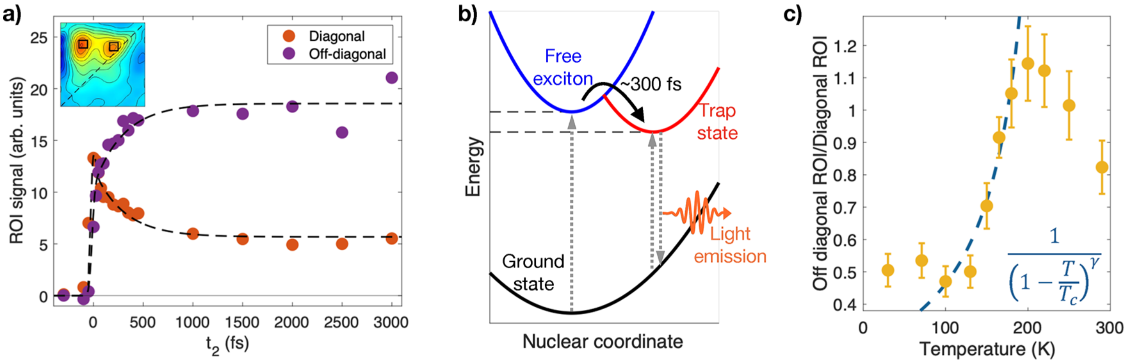

Figure 5. (a) t_2 dynamics of the 2DES signal measured at 200 K and integrated over the two regions of interest depicted in the top left inset, which select the diagonal (orange) and off-diagonal (purple) structures. (b) Sketch of the energy level structure and population dynamics of trap states originating from defects or self-trapped excitons. (c) Temperature dependence of the off-diagonal spectral feature at $t_2 = 0$ fs as compared to the diagonal excitonic resonance. The yellow markers report the ratio between the signal intensities obtained from the integration of the 2D spectra over the areas indicated in the inset of Figure 5a. The blue dashed line indicates the divergence of a second-order phase transition order parameter scaling as $(1 - T/T_c)^{-\gamma}$; here $\gamma = 1$ and $T_c = 240$ K.

temperature for the symmetry-breaking structural phase transition undergone by FAPI. The transition from the high-temperature cubic phase (space group $Pm\bar{3}m$) to the low-T tetragonal phase (space group $P4/mbm$) occurs at $T_c^{\text{bulk}} \simeq 285$ K in the bulk material,[55,56] and at smaller temperature in perovskite nanocubes.[57] For 10 nm nanocubes we can expect a ~15% decrease in T_c, that corresponds to ~240 K. Therefore, the anomalous behavior in $\Gamma_{\text{exc}}(T)$ emerging at 250 K suggests a suppression of the exciton−phonon interaction in the high-temperature structural cubic phase. More specifically, we note that the second-order structural phase transition from tetragonal to cubic at T_c is accompanied by a symmetry increase, as shown in Figure 4b. The reduction of the unit cell in the high-T cubic phase implies the reduction of the number of optical phonon modes from 36 to 18,[58] thus, limiting the phononic channels at $E_{\text{OP}} \simeq 17$ meV available for the excitonic decoherence.

2DES further snaps the subsequent formation of the long-lived states that are responsible for the slower emission of light under the form of fluorescence (see the photoluminescence spectrum in Supporting Information, Section S1-D). For this aim, we analyze the off-diagonal structure that appears in the 2D spectra shown in Figure 2 after a few picoseconds at $\hbar\omega_1 \simeq 1.72$ eV and $\hbar\omega_3 \simeq 1.61$ eV coordinates. This off-diagonal feature can not be associated with multiexciton states such as biexcitons because of the large energy separation from the diagonal structure (100 meV) and the absence of superlinear fluence dependence (see Supporting Information, Section S5). Interpretation of the two spectral features (diagonal and off-diagonal) as originating from a charge transfer between two coexisting crystal structure phases, as previously done in ref 28 for MAPI thin films, is incompatible with XRD data showing tetragonal lattice at low-T and purely cubic crystal structure at room temperature (see Supporting Information, Section S1-A). Significant information about the nature of this low-energy response can be obtained from its dynamics compared to the excitonic one. Figure 5a displays the dynamics of the two different spectral features obtained by integrating the 2D spectra over two different selected regions of interest, one centered on top of the diagonal and the other centered on the off-diagonal structures (see the inset of Figure 5a). The off-diagonal structure shows an ~300 fs build-up time, which coincides with the decay of the diagonal signal, as evidenced by the exponential fit reported in Figure 5a. This finding demonstrates that the off-diagonal structure is a long-lived state that forms after the relaxation of the initial excitonic population. This long-lived state is in turn responsible for the slower light emission, which takes place several tens of picoseconds after the initial photoexcitation.[10,28] We note that the dynamics reported in Figure 3f are compatible with what is reported in Figure 5a because in the former case, the amplitude is obtained from integration over the whole antidiagonal spectral range, whereas in the latter the integration was performed on a fixed squared area where the diagonal peak broadening caused by the rise of the biexciton component is not taken into account. This transfer of occupied states from free excitons to lower energy states is typical of trap states that get populated following the mechanism sketched in Figure 5b.[19,59,60] Such trap states can originate when the coupling between charge carriers and a local structural distortion of the lattice decreases the energy of the system.

One possible origin of trap states is related to the presence of static intrinsic defects, such as local lattice perturbations, structural disorder and vacancies.[60,61] Another possibility is that the off-diagonal structure is associated with the formation of metastable STE, i.e., localized excitons dressed by a phonon mode, most likely involving the I−Pb−I bending. Indeed, we note that the build-up time (300 fs) of the off-diagonal structure is very close to half of the period of the optical modes at ≃7 meV, which involve the halide-lead-halide bending (see Figure 4b)[53] that has been shown to be closely coupled with photoexcited excitons.[62] In general, STE formation is facilitated in solid systems displaying soft lattice, strong exciton−phonon coupling, large lattice constants and reduced electronic dimensionality.[63] These properties are often found in halide perovskites, which typically display strong electron−phonon interactions and soft lattice,[64] and in FAPI superlattices, in particular, where the formamidinium cation represents a large cation molecule as compared to MAPI or all-metal halide perovskites[25] and where the nanocube synthesis reduces the dimensionality of the system to quasi 0D due to exciton quantum confinement. STE usually results in broad emission peaks,[63] consistently with what is observed from room-temperature photoluminescence on the FAPI superlattices investigated in this work (see Supporting Information, Section S1-D). The formation of STE is also suggested by the temperature dependence of the off-diagonal structure, as reported in Figure 5c for a fixed time delay $t_2 = 0$ fs. Starting from cryogenic temperature we clearly observe a significant increase of the intensity of the off-diagonal peak as the temperature is increased, with tendency to diverge when the critical temperature of the tetragonal to cubic transition is approached. The experimental data are fitted with the function $(1 - T/T_c)^\gamma$ in order to determine the critical exponent. The data are compatible with $\gamma = 1$, which is the mean-field critical exponent of compressibility across a second-order phase transition. This result suggests that the softening of the lattice and, more specifically, of the ≃7 meV phonons responsible for the I−Pb−I bending, which softens across the tetragonal-to-cubic transition, strongly favors the formation of STE with a binding energy as large as ≃100 meV. We also note that the 2D spectra contain a weak diagonal signal at $\hbar\omega_1 = \hbar\omega_3 \simeq 1.61$ eV (see Figure S10, Supporting Information), which displays a temperature-dependent behavior similar to the off-diagonal component, thus indicating the possibility of direct excitation of this phonon-mediated transition, which consists in the simultaneous absorption of a photon and the local lattice distortion related to the STE. The lower intensity of the diagonal component as compared to the off-diagonal peak could be related to the scaling of the signal intensity with the dipole strength. Since the diagonal signal scales with the fourth power of the dipole strength, while the off-diagonal cross peak scales with the second power, small dipole strength of the trap state compared to the main excitonic line can result in the suppression of diagonal features in the 2DES spectra, despite the off-diagonal peak being clearly visible.[65,66] The spectrum of the laser excitation (see Supporting Information, Figure S8b) can also play a role in scaling down the intensity of the measured signal at small photon energies ($\hbar\omega_1 \sim 1.61$ eV),[65,67] thus, further suppressing diagonal features.

■ CONCLUSIONS

In conclusion, our 2DES study has unveiled the complex hierarchy of the photophysics in FAPI superlattices. The initial excitons very rapidly (≃ 40 fs) decay forming an incoherent gas of biexcitons. Within hundreds of femtoseconds, the optical excitations form trap states that originate from defects or lattice distortions causing self-trapping of excitons. The large binding energy and the spatial localization protect these new and long-lived states that are responsible for the subsequent fluorescent emission.[68,69] We note that a direct comparison with disordered FAPI nanocrystals cannot be performed due to the strong signal suppression in disordered films (Supporting Information Section S7). The way the ordered arrangement of the nanocubes enhances the signal calls for further investigation that goes beyond the scope of the present work. Nevertheless, the present results suggest that the short excitonic decoherence time prevents the onset of collective superradiant emission, in contrast with observations in inorganic superlattices.[10−14] At the same time, the strong coupling with the optical phonons, combined with the lattice softening across a continuous structural phase transition, offers a new tool to manipulate the excitonic/biexcitonic coherent dynamics, as well as the down-conversion into trap states, which ultimately controls the collective and coherent emission properties.

■ MATERIALS AND METHODS

Sample Preparation. $FAPbI_3$ (or FAPI) nanocubes (NCs) were synthesized following the procedure reported in ref 70 with little modifications. A stock solution of oleylammonium iodide (OLAm-I) was prepared by loading 750 mg of I_2 (3 mmol), 10.5 mL of octadecene-1 (ODE, 90%), and 4.5 mL of oleylamine (OLAm, 70%) into a 40 mL vial. The solution was dried under vacuum for 15 min at room temperature (RT), for 30 min at 90 °C and then heated up to 110 °C under N_2 flow. At this temperature, the solution turned transparent light brown, which indicates the formation of oleylammonium iodide. Before using it, the OLAm-I stock solution was vigorously stirred and heated at around 80 °C since it partially solidifies at RT. In a 40 mL vial, 76 mg of lead acetate trihydrate ($PbAc_2\cdot 3H_2O$, 0.2 mmol) and 62 mg of formamidinium acetate (FAAc, 0.6 mmol) were combined with 5 mL of ODE and 3 mL of oleic acid (OA). The mixture was dried under vacuum at RT for 15 min and then at 125 °C for 30 min. Next, under N_2 flow, the FA-based mixture was brought down to 120 °C and 1.5 mL of preheated OLAm-I precursor solution were injected. The reaction mixture was cooled down after 10 s with an ice−water bath. The crude solution was centrifuged at 4000 rpm for 6 min and the supernatant was discarded. Then the wet solid was centrifuged again at 4000 rpm for 3 min, the remaining liquid was removed with a 100 μL mechanical micropipette, and the step was repeated again, this time using a cotton swab to collect the residual liquid. The remaining solid was dissolved in 1 mL of toluene, centrifuged at 6000 rpm, and filtered through 0.45 μm hydrophobic PTFE syringe filter to eliminate any residual aggregates. Nanocubes superlattices were prepared by slow solvent evaporation on 1 cm × 1 cm monocrystalline Si substrates cleaned by rinsing with methanol and acetone and dried with paper tissues and by blowing N_2. The substrates were placed inside a Petri dish, and 30 μL of stock solution of NCs were drop-casted on each of them, so to have a total amount of solution equal to ≈90 μL. After the solvent was completely evaporated (≈12 h), films were considered ready for optical experiment and characterization (Supporting Information, Section S1).

2DES Optical Setup. A sketch of the 2DES setup is reported in Supporting Information, Figure S8a. Both pump and probe pulses are generated by a home-built noncollinear optical parametric amplifier (NOPA), seeded by a Yb:KGW laser system (Pharos by Light Conversion) emitting 300 fs pulses at 1030 nm (1.2 eV). The NOPA output signal is tuned at 1.7 eV central energy (see Figure S8b) and compressed to 30 fs time duration (fwhm) by multiple bounces on a pair of chirped mirrors. Pump and probe beams are obtained by dividing the NOPA output by means of a beam splitter. The pair of phase-coherent excitation pulses are generated by a common-path birefringent interferometer (GEMINI 2D by NIREOS) based on the Translating-Wedge-Based Identical Pulses eNcoding System (TWINS) scheme.[39] A two-prism compressor compensates for the additional dispersion introduced in the pump pulses by the GEMINI 2D interferometer and other optical elements on the pump beam (beam splitter, half-waveplate, and cryostat window). Similarly, a two-prism compressor is employed for fine compensation of dispersing elements on the probe beam, namely, a half-waveplate and the cryostat window. Pump and probe pulses, orthogonally polarized in order to minimize pump scattering, are then focused onto the sample by two concave mirrors, resulting in a partially collinear 2DES scheme (collinear pump pulses and noncollinear probe propagation). The focused spot size is 170 μm × 230 μm for the pump beam and 70 μm × 70 μm for the probe beam. The pump−probe time delay t_2 is controlled through a linearly motorized stage and is scanned between −500 fs and 4 ps. The delay between the two pump pulses, t_1 is controlled by varying the insertion of the GEMINI 2D birefringent wedges on the beam path, and it is continuously scanned between −55 and 110 fs for each measured t_2.

The 2DES signal propagating collinearly with the probe beam is collected in a reflection geometry. The transient reflectivity signal at each (t_1,t_2) is obtained by modulating the pump excitation with a mechanical chopper and performing lock-in acquisition of the reflected probe.[40] Spectral resolution along the detection frequency axis is achieved by employing a GEMINI interferometer (NIREOS) that generates the probe interferogram and returns the transient reflectivity spectrum upon Fourier transform computation.

The pump fluence F can be continuously varied between 0 and 230 μJ/cm^2 (as measured at $t_1 = 0$) by rotating a half-waveplate positioned on the pump beam path before the GEMINI 2D, whose polarizers select the 45° polarized component of the light. For the measurements presented in this work, the laser repetition rate was set to 40 kHz. A different repetition rate, selected by means of a pulse picker that allows keeping unvaried the energy per pulse, was employed for fluence-dependent studies where the repetition rate was increased up to 200 kHz as the excitation intensity was decreased in order to maintain the average power at the sample constant throughout the fluence scan.

Temperature-dependent investigations were performed by mounting the samples inside a closed-cycle helium cryostat that allows performing ultrafast optical spectroscopy experiments at temperatures between 20 and 300 K.

■ ASSOCIATED CONTENT

Supporting Information

The Supporting Information is available free of charge at https://pubs.acs.org/doi/10.1021/acsphotonics.4c00105.

> Samples preparation; XRD patterns of FAPI superlattices; Temperature-dependent XRD patterns of FAPI nanocubes; TEM characterization; absorbance and photoluminescence spectra; Scheme of the 2DES experimental setup; Simulation of the dynamics of exciton decay and biexciton formation; Details of multipeak fitting analysis of 2DES spectra antidiagonal cuts; 2DES fluence-dependent data at t_2 = 3 ps; 2DES data on disordered FAPI nanocubes; 2DES data in transmission geometry; Exciton density estimate (PDF)

■ AUTHOR INFORMATION

Corresponding Authors

Alessandra Milloch − *Department of Mathematics and Physics, Università Cattolica del Sacro Cuore, Brescia I-25133, Italy; ILAMP (Interdisciplinary Laboratories for Advanced Materials Physics), Università Cattolica del Sacro Cuore, Brescia I-25133, Italy; Department of Physics and Astronomy, KU Leuven, B-3001 Leuven, Belgium;* orcid.org/0000-0003-1790-0462; Email: alessandra.milloch@unicatt.it

Claudio Giannetti − *Department of Mathematics and Physics, Università Cattolica del Sacro Cuore, Brescia I-25133, Italy; ILAMP (Interdisciplinary Laboratories for Advanced Materials Physics), Università Cattolica del Sacro Cuore, Brescia I-25133, Italy; CNR-INO (National Institute of Optics), 25123 Brescia, Italy;* orcid.org/0000-0003-2664-9492; Email: claudio.giannetti@unicatt.it

Authors

Umberto Filippi − *Italian Institute of Technology (IIT), Genova 16163, Italy*

Paolo Franceschini − *CNR-INO (National Institute of Optics), 25123 Brescia, Italy; Department of Information Engineering, University of Brescia, Brescia I-25123, Italy;* orcid.org/0000-0001-5405-7668

Selene Mor − *Department of Mathematics and Physics, Università Cattolica del Sacro Cuore, Brescia I-25133, Italy; ILAMP (Interdisciplinary Laboratories for Advanced Materials Physics), Università Cattolica del Sacro Cuore, Brescia I-25133, Italy;* orcid.org/0000-0002-9067-8055

Stefania Pagliara − *Department of Mathematics and Physics, Università Cattolica del Sacro Cuore, Brescia I-25133, Italy; ILAMP (Interdisciplinary Laboratories for Advanced Materials Physics), Università Cattolica del Sacro Cuore, Brescia I-25133, Italy;* orcid.org/0000-0003-2966-3361

Gabriele Ferrini − *Department of Mathematics and Physics, Università Cattolica del Sacro Cuore, Brescia I-25133, Italy; ILAMP (Interdisciplinary Laboratories for Advanced Materials Physics), Università Cattolica del Sacro Cuore, Brescia I-25133, Italy;* orcid.org/0000-0002-5062-9099

Franco V. A. Camargo − *IFN-CNR, I-20133 Milano, Italy;* orcid.org/0000-0001-8312-7899

Giulio Cerullo − *IFN-CNR, I-20133 Milano, Italy; Department of Physics, Politecnico di Milano, I-20133 Milano, Italy;* orcid.org/0000-0002-9534-2702

Dmitry Baranov − *Italian Institute of Technology (IIT), Genova 16163, Italy; Division of Chemical Physics, Department of Chemistry, Lund University, SE-221 00 Lund, Sweden;* orcid.org/0000-0001-6439-8132

Liberato Manna − *Italian Institute of Technology (IIT), Genova 16163, Italy;* orcid.org/0000-0003-4386-7985

Complete contact information is available at: https://pubs.acs.org/10.1021/acsphotonics.4c00105

Funding

C.G., P.F., A.M., and S.M. acknowledge financial support from MIUR through the PRIN 2017 (Prot. 20172H2SC4 005) and PRIN 2020 (Prot. 2020JLZ52N 003) programs and from the European Union - Next Generation EU through the MUR-PRIN2022 (Prot. 20228YCYY7) program. C.G., S.P., and G.F. acknowledge support from Università Cattolica del Sacro Cuore through D.1, D.2.2, and D.3.1 Grants. S.M. acknowledges partial financial support through the grant "Finanziamenti ponte per bandi esterni" from Università Cattolica del Sacro Cuore. G.C. acknowledges financial support by the European Union's NextGenerationEU Programme with the I-PHOQS Infrastructure [IR0000016, ID D2B8D520, CUP B53C22001750006] "Integrated infrastructure initiative in Photonic and Quantum Sciences".

Notes

The authors declare no competing financial interest.

■ REFERENCES

(1) Herz, L. M. Charge-carrier dynamics in organic-inorganic metal halide perovskites. *Annu. Rev. Phys. Chem.* **2016**, *67*, 65−89.

(2) Kanemitsu, Y. Luminescence spectroscopy of lead-halide perovskites: materials properties and application as photovoltaic devices. *J. Mater. Chem. C* **2017**, *5*, 3427−3437.

(3) Quan, L. N.; Rand, B. P.; Friend, R. H.; Mhaisalkar, S. G.; Lee, T.-W.; Sargent, E. H. Perovskites for next-generation optical sources. *Chem. Rev.* **2019**, *119*, 7444−7477.

(4) Stranks, S. D.; Snaith, H. J. Metal-halide perovskites for photovoltaic and light-emitting devices. *Nature Nanotechnol.* **2015**, *10*, 391−402.

(5) Shamsi, J.; Urban, A. S.; Imran, M.; De Trizio, L.; Manna, L. Metal halide perovskite nanocrystals: synthesis, post-synthesis modifications, and their optical properties. *Chem. Rev.* **2019**, *119*, 3296−3348.

(6) Jurow, M. J.; Lampe, T.; Penzo, E.; Kang, J.; Koc, M. A.; Zechel, T.; Nett, Z.; Brady, M.; Wang, L.-W.; Alivisatos, A. P.; et al. Tunable anisotropic photon emission from self-organized $CsPbBr_3$ perovskite nanocrystals. *Nano Lett.* **2017**, *17*, 4534−4540.

(7) Tong, Y.; Yao, E.-P.; Manzi, A.; Bladt, E.; Wang, K.; Döblinger, M.; Bals, S.; Müller-Buschbaum, P.; Urban, A. S.; Polavarapu, L.; et al. Spontaneous self-assembly of perovskite nanocrystals into electronically coupled supercrystals: toward filling the green gap. *Adv. Mater.* **2018**, *30*, 1801117.

(8) Baranov, D.; Toso, S.; Imran, M.; Manna, L. Investigation into the photoluminescence red shift in cesium lead bromide nanocrystal superlattices. *J. Phys. Chem. Lett.* **2019**, *10*, 655−660.

(9) Cherniukh, I.; Rainò, G.; Stöferle, T.; Burian, M.; Travesset, A.; Naumenko, D.; Amenitsch, H.; Erni, R.; Mahrt, R. F.; Bodnarchuk, M. I.; et al. Perovskite-type superlattices from lead halide perovskite nanocubes. *Nature* **2021**, *593*, 535−542.

(10) Rainò, G.; Becker, M. A.; Bodnarchuk, M. I.; Mahrt, R. F.; Kovalenko, M. V.; Stöferle, T. Superfluorescence from lead halide perovskite quantum dot superlattices. *Nature* **2018**, *563*, 671−675.

(11) Zhou, C.; Zhong, Y.; Dong, H.; Zheng, W.; Tan, J.; Jie, Q.; Pan, A.; Zhang, L.; Xie, W. Cooperative excitonic quantum ensemble in perovskite-assembly superlattice microcavities. *Nat. Commun.* **2020**, *11*, 329.

(12) Krieg, F.; Sercel, P. C.; Burian, M.; Andrusiv, H.; Bodnarchuk, M. I.; Stöferle, T.; Mahrt, R. F.; Naumenko, D.; Amenitsch, H.; Rainò, G.; et al. Monodisperse long-chain sulfobetaine-capped $CsPbBr_3$ nanocrystals and their superfluorescent assemblies. *ACS Central Sci.* **2021**, *7*, 135−144.

(13) Pashaei Adl, H.; Gorji, S.; Muñoz-Matutano, G.; Gualdrón-Reyes, A. F.; Suárez, I.; Chirvony, V. S.; Mora-Seró, I.; Martínez-Pastor, J. P. Superradiance Emission and Its Thermal Decoherence in Lead Halide Perovskites Superlattices. *Adv. Opt. Mater.* **2023**, *11*, 2202497.

(14) Milloch, A.; Filippi, U.; Franceschini, P.; Galvani, M.; Mor, S.; Pagliara, S.; Ferrini, G.; Banfi, F.; Capone, M.; Baranov, D.; Manna, L.; Giannetti, C. Halide Perovskite Artificial Solids as a New Platform to Simulate Collective Phenomena in Doped Mott Insulators. *Nano Lett.* **2023**, *23*, 10617−10624.

(15) Cong, K.; Zhang, Q.; Wang, Y.; Noe, G. T.; Belyanin, A.; Kono, J. Dicke superradiance in solids. *JOSA B* **2016**, *33*, C80−C101.

(16) Mattiotti, F.; Kuno, M.; Borgonovi, F.; Jankó, B.; Celardo, G. L. Thermal decoherence of superradiance in lead halide perovskite nanocrystal superlattices. *Nano Lett.* **2020**, *20*, 7382−7388.

(17) Ghonge, S.; Engel, D.; Mattiotti, F.; Celardo, G. L.; Kuno, M.; Jankó, B. Enhanced robustness and dimensional crossover of superradiance in cuboidal nanocrystal superlattices. *Phys. Rev. Res.* **2023**, *5*, 023068.

(18) Blach, D. D.; Lumsargis, V. A.; Clark, D. E.; Chuang, C.; Wang, K.; Dou, L.; Schaller, R. D.; Cao, J.; Li, C. W.; Huang, L. Superradiance and exciton delocalization in perovskite quantum dot superlattices. *Nano Lett.* **2022**, *22*, 7811−7818.

(19) Smith, M. D.; Karunadasa, H. I. White-light emission from layered halide perovskites. *Acc. Chem. Res.* **2018**, *51*, 619−627.

(20) Li, S.; Luo, J.; Liu, J.; Tang, J. Self-trapped excitons in all-inorganic halide perovskites: fundamentals, status, and potential applications. *J. Phys. Chem. Lett.* **2019**, *10*, 1999−2007.

(21) Manser, J. S.; Christians, J. A.; Kamat, P. V. Intriguing optoelectronic properties of metal halide perovskites. *Chem. Rev.* **2016**, *116*, 12956−13008.

(22) Chen, Q.; De Marco, N.; Yang, Y. M.; Song, T.-B.; Chen, C.-C.; Zhao, H.; Hong, Z.; Zhou, H.; Yang, Y. Under the spotlight: The organic−inorganic hybrid halide perovskite for optoelectronic applications. *Nano Today* **2015**, *10*, 355−396.

(23) Fang, H.-H.; Protesescu, L.; Balazs, D. M.; Adjokatse, S.; Kovalenko, M. V.; Loi, M. A. Exciton Recombination in Formamidinium Lead Triiodide: Nanocrystals versus Thin Films. *Small* **2017**, *13*, 1700673.

(24) Levchuk, I.; Osvet, A.; Tang, X.; Brandl, M.; Perea, J. D.; Hoegl, F.; Matt, G. J.; Hock, R.; Batentschuk, M.; Brabec, C. J. Brightly luminescent and color-tunable formamidinium lead halide perovskite $FAPbX_3$ (X= Cl, Br, I) colloidal nanocrystals. *Nano Lett.* **2017**, *17*, 2765−2770.

(25) Tan, M.; Chen, B.; Zhang, Y.; Ni, M.; Wang, W.; Zhang, H.; Zhou, Q.; Bao, Y.; Wang, Y. Temperature-dependent dynamic carrier process of $FAPbI_3$ nanocrystals' film. *J. Phys. Chem. C* **2020**, *124*, 5093−5098.

(26) Fang, H.-H.; Wang, F.; Adjokatse, S.; Zhao, N.; Even, J.; Antonietta Loi, M. Photoexcitation dynamics in solution-processed formamidinium lead iodide perovskite thin films for solar cell applications. *Light: Sci. Appl.* **2016**, *5*, e16056−e16056.

(27) Yamada, Y.; Nakamura, T.; Endo, M.; Wakamiya, A.; Kanemitsu, Y. Photocarrier recombination dynamics in perovskite $CH_3NH_3PbI_3$ for solar cell applications. *J. Am. Chem. Soc.* **2014**, *136*, 11610−11613.

(28) Phuong, L. Q.; Yamada, Y.; Nagai, M.; Maruyama, N.; Wakamiya, A.; Kanemitsu, Y. Free carriers versus excitons in $CH_3NH_3PbI_3$ perovskite thin films at low temperatures: charge transfer from the orthorhombic phase to the tetragonal phase. *J. Phys. Chem. Lett.* **2016**, *7*, 2316−2321.

(29) Tahara, H.; Endo, M.; Wakamiya, A.; Kanemitsu, Y. Experimental evidence of localized shallow states in orthorhombic phase of $CH_3NH_3PbI_3$ perovskite thin films revealed by photocurrent beat spectroscopy. *J. Phys. Chem. C* **2016**, *120*, 5347−5352.

(30) Li, Y.; Allegro, I.; Kaiser, M.; Malla, A. J.; Richards, B. S.; Lemmer, U.; Paetzold, U. W.; Howard, I. A. Exciton versus free carrier emission: Implications for photoluminescence efficiency and amplified spontaneous emission thresholds in quasi-2D and 3D perovskites. *Mater. Today* **2021**, *49*, 35−47.

(31) Sutherland, B. R.; Sargent, E. H. Perovskite photonic sources. *Nat. Photonics* **2016**, *10*, 295−302.

(32) Zhang, S.; Jin, L.; Lu, Y.; Zhang, L.; Yang, J.; Zhao, Q.; Sun, D.; Thompson, J. J.; Yuan, B.; Ma, K.; et al. Moiré superlattices in twisted two-dimensional halide perovskites. *Nat. Mater.* **2024**, 1−8.

(33) Jonas, D. M. Two-dimensional femtosecond spectroscopy. *Annu. Rev. Phys. Chem.* **2003**, *54*, 425−463.

(34) Cho, M. Coherent two-dimensional optical spectroscopy. *Chem. Rev.* **2008**, *108*, 1331−1418.

(35) Mukamel, S. Multidimensional femtosecond correlation spectroscopies of electronic and vibrational excitations. *Annu. Rev. Phys. Chem.* **2000**, *51*, 691−729.

(36) Fuller, F. D.; Ogilvie, J. P. Experimental implementations of two-dimensional Fourier transform electronic spectroscopy. *Annu. Rev. Phys. Chem.* **2015**, *66*, 667−690.

(37) Tollerud, J. O.; Davis, J. A. Coherent multi-dimensional spectroscopy: Experimental considerations, direct comparisons and new capabilities. *Prog. Quantum Electron.* **2017**, *55*, 1−34.

(38) Oriana, A.; Réhault, J.; Preda, F.; Polli, D.; Cerullo, G. Scanning Fourier transform spectrometer in the visible range based on birefringent wedges. *JOSA A* **2016**, *33*, 1415−1420.

(39) Brida, D.; Manzoni, C.; Cerullo, G. Phase-locked pulses for two-dimensional spectroscopy by a birefringent delay line. *Opt. Lett.* **2012**, *37*, 3027−3029.

(40) Preda, F.; Kumar, V.; Crisafi, F.; Figueroa del Valle, D. G.; Cerullo, G.; Polli, D. Broadband pump-probe spectroscopy at 20-MHz modulation frequency. *Opt. Lett.* **2016**, *41*, 2970−2973.

(41) Aneesh, J.; Swarnkar, A.; Kumar Ravi, V.; Sharma, R.; Nag, A.; Adarsh, K. Ultrafast exciton dynamics in colloidal $CsPbBr_3$ perovskite nanocrystals: Biexciton effect and Auger recombination. *J. Phys. Chem. C* **2017**, *121*, 4734−4739.

(42) Cho, K.; Yamada, T.; Tahara, H.; Tadano, T.; Suzuura, H.; Saruyama, M.; Sato, R.; Teranishi, T.; Kanemitsu, Y. Luminescence fine structures in single lead halide perovskite nanocrystals: size dependence of the exciton−phonon coupling. *Nano Lett.* **2021**, *21*, 7206−7212.

(43) Huang, X.; Chen, L.; Zhang, C.; Qin, Z.; Yu, B.; Wang, X.; Xiao, M. Inhomogeneous biexciton binding in perovskite semiconductor nanocrystals measured with two-dimensional spectroscopy. *J. Phys. Chem. Lett.* **2020**, *11*, 10173−10181.

(44) Shulenberger, K. E.; Ashner, M. N.; Ha, S. K.; Krieg, F.; Kovalenko, M. V.; Tisdale, W. A.; Bawendi, M. G. Setting an upper bound to the biexciton binding energy in $CsPbBr_3$ perovskite nanocrystals. *J. Phys. Chem. Lett.* **2019**, *10*, 5680−5686.

(45) Dostál, J.; Fennel, F.; Koch, F.; Herbst, S.; Würthner, F.; Brixner, T. Direct observation of exciton-exciton interactions. *Nat. Commun.* **2018**, *9*, 2466.

(46) Kriete, B.; Lüttig, J.; Kunsel, T.; Malý, P.; Jansen, T. L.; Knoester, J.; Brixner, T.; Pshenichnikov, M. S. Interplay between structural hierarchy and exciton diffusion in artificial light harvesting. *Nat. Commun.* **2019**, *10*, 4615.

(47) Siemens, M. E.; Moody, G.; Li, H.; Bristow, A. D.; Cundiff, S. T. Resonance lineshapes in two-dimensional Fourier transform spectroscopy. *Opt. Express* **2010**, *18*, 17699−17708.

(48) Russo, M.; McGhee, K. E.; Virgili, T.; Lidzey, D. G.; Cerullo, G.; Maiuri, M. Dephasing processes in the molecular dye lumogen-f orange characterized by two-dimensional electronic spectroscopy. *Molecules* **2022**, *27*, 7095.

(49) Lee, J.; Koteles, E. S.; Vassell, M. Luminescence linewidths of excitons in GaAs quantum wells below 150 K. *Phys. Rev. B* **1986**, *33*, 5512.

(50) Fu, M.; Tamarat, P.; Trebbia, J.-B.; Bodnarchuk, M. I.; Kovalenko, M. V.; Even, J.; Lounis, B. Unraveling exciton−phonon coupling in individual $FAPbI_3$ nanocrystals emitting near-infrared single photons. *Nat. Commun.* **2018**, *9*, 3318.

(51) Ferreira, A.; Paofai, S.; Létoublon, A.; Ollivier, J.; Raymond, S.; Hehlen, B.; Rufflé, B.; Cordier, S.; Katan, C.; Even, J.; et al. Direct evidence of weakly dispersed and strongly anharmonic optical phonons in hybrid perovskites. *Commun. Phys.* **2020**, *3*, 48.

(52) Yuan, F.; Wu, Z.; Dong, H.; Xi, J.; Xi, K.; Divitini, G.; Jiao, B.; Hou, X.; Wang, S.; Gong, Q. High stability and ultralow threshold amplified spontaneous emission from formamidinium lead halide perovskite films. *J. Phys. Chem. C* **2017**, *121*, 15318−15325.

(53) Quarti, C.; Grancini, G.; Mosconi, E.; Bruno, P.; Ball, J. M.; Lee, M. M.; Snaith, H. J.; Petrozza, A.; De Angelis, F. The Raman spectrum of the $CH_3NH_3PbI_3$ hybrid perovskite: interplay of theory and experiment. *J. Phys. Chem. Lett.* **2014**, *5*, 279−284.

(54) Park, M.; Kornienko, N.; Reyes-Lillo, S. E.; Lai, M.; Neaton, J. B.; Yang, P.; Mathies, R. A. Critical role of methylammonium librational motion in methylammonium lead iodide ($CH_3NH_3PbI_3$) perovskite photochemistry. *Nano Lett.* **2017**, *17*, 4151−4157.

(55) Fabini, D. H.; Stoumpos, C. C.; Laurita, G.; Kaltzoglou, A.; Kontos, A. G.; Falaras, P.; Kanatzidis, M. G.; Seshadri, R. Reentrant structural and optical properties and large positive thermal expansion in perovskite formamidinium lead iodide. *Angew. Chem.* **2016**, *128*, 15618−15622.

(56) Weber, O. J.; Ghosh, D.; Gaines, S.; Henry, P. F.; Walker, A. B.; Islam, M. S.; Weller, M. T. Phase behavior and polymorphism of formamidinium lead iodide. *Chem. Mater.* **2018**, *30*, 3768−3778.

(57) Liu, L.; Zhao, R.; Xiao, C.; Zhang, F.; Pevere, F.; Shi, K.; Huang, H.; Zhong, H.; Sychugov, I. Size-dependent phase transition in perovskite nanocrystals. *J. Phys. Chem. Lett.* **2019**, *10*, 5451−5457.

(58) Maalej, A.; Abid, Y.; Kallel, A.; Daoud, A.; Lautié, A.; Romain, F. Phase transitions and crystal dynamics in the cubic perovskite $CH_3NH_3PbCl_3$. *Solid State Commun.* **1997**, *103*, 279−284.

(59) Wright, A. D.; Milot, R. L.; Eperon, G. E.; Snaith, H. J.; Johnston, M. B.; Herz, L. M. Band-tail recombination in hybrid lead iodide perovskite. *Adv. Funct. Mater.* **2017**, *27*, 1700860.

(60) Grandhi, G. K.; Dhama, R.; Viswanath, N. S. M.; Lisitsyna, E. S.; Al-Anesi, B.; Dana, J.; Sugathan, V.; Caglayan, H.; Vivo, P. Role of Self-Trapped Excitons in the Broadband Emission of Lead-Free Perovskite-Inspired Cu_2AgBiI_6. *J. Phys. Chem. Lett.* **2023**, *14*, 4192−4199.

(61) Luo, J.; Wang, X.; Li, S.; Liu, J.; Guo, Y.; Niu, G.; Yao, L.; Fu, Y.; Gao, L.; Dong, Q.; et al. Efficient and stable emission of warm-white light from lead-free halide double perovskites. *Nature* **2018**, *563*, 541−545.

(62) Yazdani, N.; Bodnarchuk, M. I.; Bertolotti, F.; Masciocchi, N.; Fureraj, I.; Guzelturk, B.; Cotts, B. L.; Zajac, M.; Rainò, G.; Jansen, M.; et al. Coupling to octahedral tilts in halide perovskite nanocrystals induces phonon-mediated attractive interactions between excitons. *Nat. Phys.* **2024**, *20*, 47−53.

(63) Tan, J.; Li, D.; Zhu, J.; Han, N.; Gong, Y.; Zhang, Y. Self-trapped excitons in soft semiconductors. *Nanoscale* **2022**, *14*, 16394−16414.

(64) Yamada, Y.; Kanemitsu, Y. Electron-phonon interactions in halide perovskites. *NPG Asia Materials* **2022**, *14*, 48.

(65) Tollerud, J. O.; Cundiff, S. T.; Davis, J. A. Revealing and characterizing dark excitons through coherent multidimensional spectroscopy. *Phys. Rev. Lett.* **2016**, *117*, 097401.

(66) Camargo, F. V.; Nagahara, T.; Feldmann, S.; Richter, J. M.; Friend, R. H.; Cerullo, G.; Deschler, F. Dark subgap states in metal-halide perovskites revealed by coherent multidimensional spectroscopy. *J. Am. Chem. Soc.* **2020**, *142*, 777−782.

(67) Camargo, F. V. A.; Grimmelsmann, L.; Anderson, H. L.; Meech, S. R.; Heisler, I. A. Resolving vibrational from electronic coherences in two-dimensional electronic spectroscopy: The role of the laser spectrum. *Phys. Rev. Lett.* **2017**, *118*, 033001.

(68) Neukirch, A. J.; Nie, W.; Blancon, J.-C.; Appavoo, K.; Tsai, H.; Sfeir, M. Y.; Katan, C.; Pedesseau, L.; Even, J.; Crochet, J. J.; Gupta, G.; Mohite, A. D.; Tretiak, S. Polaron Stabilization by Cooperative Lattice Distortion and Cation Rotations in Hybrid Perovskite Materials. *Nano Lett.* **2016**, *16*, 3809−3816.

(69) Zhu, H.; Miyata, K.; Fu, Y.; Wang, J.; Joshi, P. P.; Niesner, D.; Williams, K. W.; Jin, S.; Zhu, X.-Y. Screening in crystalline liquids protects energetic carriers in hybrid perovskites. *Science* **2016**, *353*, 1409−1413.

(70) Akkerman, Q. A.; Martinez-Sarti, L.; Goldoni, L.; Imran, M.; Baranov, D.; Bolink, H. J.; Palazon, F.; Manna, L. Molecular Iodine for a General Synthesis of Binary and Ternary Inorganic and Hybrid Organic−Inorganic Iodide Nanocrystals. *Chem. Mater.* **2018**, *30*, 6915−6921.